Strain accommodation by magmatism and faulting as rifting proceeds to breakup: Seismicity of the northern Ethiopian rift

Strain accommodation by magmatism and faulting as rifting proceeds to breakup: Seismicity of the northern Ethiopian rift

Derek Keir,[1] C. J. Ebinger,[1] G. W. Stuart,[2] E. Daly,[3] and A. Ayele[4]

Received 24 March 2005; revised 1 December 2005; accepted 2 February 2006; published 26 May 2006.

[1] The volcanically active Main Ethiopian rift (MER) marks the transition from continental rifting in the East African rift to incipient seafloor spreading in Afar. We use new seismicity data to investigate the distribution of strain and its relationship with magmatism immediately prior to continental breakup. From October 2001 to January 2003, seismicity was recorded by up to 179 broadband instruments that covered a 250 km × 350 km area. A total of 1957 earthquakes were located within the network, a selection of which was used for accurate location with a three-dimensional velocity model and focal mechanism determination. Border faults are inactive except for a cluster of seismicity at the structurally complex intersection of the MER and the older Red Sea rift, where the Red Sea rift flank is downwarped into the younger MER. Earthquakes are localized to ~20-km-wide, right-stepping en echelon zones of Quaternary magmatism and faulting, which are underlain by mafic intrusions that rise to 8–10 km subsurface. Seismicity in these "magmatic segments" is characterized by low-magnitude swarms coincident with Quaternary faults, fissures, and chains of eruptive centers. All but three focal mechanisms show normal dip-slip motion; the minimum compressive stress is N103°E, perpendicular to Quaternary faults and aligned volcanic cones. The earthquake catalogue is complete above M_L 2.1, and the estimated b value is 1.13 ± 0.05. The seismogenic zone lies above the 20-km-wide intrusion zones; intrusion may trigger faulting in the upper crust. New and existing data indicate that during continental breakup, intrusion of magma beneath ~20-km-wide magmatic segments accommodates the majority of strain and controls the locus of seismicity and faulting in the upper crust.

Citation: Keir, D., C. J. Ebinger, G. W. Stuart, E. Daly, and A. Ayele (2006), Strain accommodation by magmatism and faulting as rifting proceeds to breakup: Seismicity of the northern Ethiopian rift, *J. Geophys. Res.*, *111*, B05314, doi:10.1029/2005JB003748.

1. Introduction

[2] Strain localizes as rifting proceeds to continental breakup, but the partitioning of strain between faults and magmatic intrusion remains controversial [e.g., *Lister et al.*, 1986; *Ebinger and Casey*, 2001]. Models of continental breakup that assume purely mechanical stretching predict strain localization along preexisting or new shear zones that may accommodate large displacements [e.g., *Lister et al.*, 1986; *Dunbar and Sawyer*, 1989]. Magmatic processes superposed on the mechanical deformation pose additional complications to our understanding of continental breakup. The magma-assisted rifting model of *Buck* [2004] shows that if a steady supply of magma is available, the release of stress and overall decrease in lithospheric strength due to diking will prevent the stress level reaching those required to activate the border faults of a rift zone. As a result, border faults become inactive and extension localizes to the zone of diking. Extension near the surface, where the brittle short-term rheology allows rapid fault slip, is accommodated by a combination of faulting and dike injection. Analysis of seismicity in a volcanically active rift setting that is near breakup provides a means to study the pattern of strain localization and assess how strain is partitioned between faulting and dike injection.

[3] The seismically and volcanically active northern Main Ethiopian rift (MER) and Afar rifts are virtually the only places worldwide where the transition between continental and oceanic rifting is exposed on land. The multidisciplinary project EAGLE (Ethiopia Afar Geoscientific Lithospheric Experiment) provides fundamental constraints on crust and upper mantle structure beneath the MER, set within a strong regional tectonic framework [e.g., *Maguire et al.*, 2003; *WoldeGabriel et al.*, 1990; *Wolfenden et al.*, 2004]. The MER is thus an ideal natural laboratory to study continental breakup processes.

[4] The EAGLE network, the largest array of seismic instruments yet deployed on the African continent, is used to analyze the distribution of local earthquakes in this

[1]Department of Geology, Royal Holloway University of London, Egham, UK.
[2]School of Earth and Environment, University of Leeds, Leeds, UK.
[3]Department of Earth and Ocean Sciences, National University of Ireland, Galway, UK.
[4]Geophysical Observatory, Addis Ababa University, Addis Ababa, Ethiopia.

0148-0227/06/2005JB003748$09.00

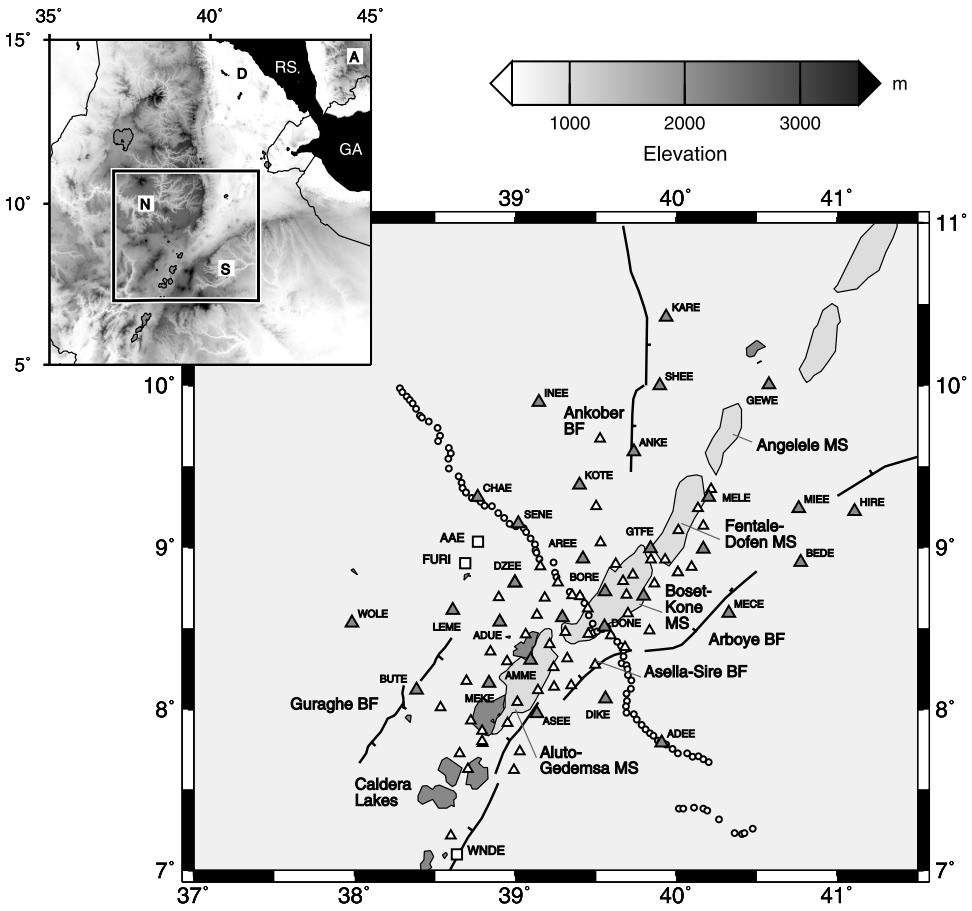

Figure 1. EAGLE permanent broadband seismic stations used for earthquake location with respect to major border faults and magmatic segments of the Main Ethiopian rift (MER). Grey triangles are phase 1 stations (October 2001 to January 2003), white triangles are phase 2 stations (October 2002 to January 2003), white circles are phase 3 stations (November 2002 to January 2003), and white squares are the IRIS GSN permanent stations FURI and permanent stations AAE and WNDE. The inset shows the topographic relief, plates, and rift zones: A, Arabia; D, Danakil; N, Nubian Plate; S, Somalian Plate; RS, Red Sea rift; GA, Gulf of Aden rift.

transitional rift zone [*Maguire et al.*, 2003] (Figure 1). Our seismicity study aims to evaluate the accommodation of strain by faulting and magmatic processes in the MER. We use accurately located hypocenters to map out variations in thickness of the seismogenic layer. Patterns of seismicity are then compared with the distribution of Quaternary faults and magmatism to distinguish between models for strain localization prior to continental breakup. Earthquake focal mechanisms are used to determine fault slip parameters and inverted for the extension direction across the Ethiopian rift. These results are then compared to global and local plate kinematic models. Our new seismicity data are interpreted in light of structural, seismic refraction/wide-angle reflection, gravity, anisotropy, and crustal and mantle tomographic studies to propose that extension via magma injection and minor faulting characterizes the late stages of continental rifting prior to breakup.

2. Tectonic Setting

[5] The Ethiopian rift system is on the Ethiopia-Yemen plateau that is thought to have developed above a mantle plume [e.g., *Schilling*, 1973; *Ebinger and Sleep*, 1998; *George et al.*, 1998]. A ~2-km-thick sequence of flood basalts and rhyolites erupted across the Ethiopia-Yemen plateau region between 45 and 22 Ma [e.g., *George et al.*, 1998; *Kieffer et al.*, 2004]. The majority erupted at ~30 Ma along the Red Sea margins [e.g., *Hofmann et al.*, 1997; *Ukstins et al.*, 2002] coincident with the opening of the Red Sea and Gulf of Aden [*Wolfenden et al.*, 2005]. Anomalously low *P* wave velocities exist in the mantle beneath Afar to depths of at least 410 km, but their connection with the profound low-velocity zone in the lower mantle beneath southern Africa is debated [e.g., *Debayle et al.*, 2001; *Benoit et al.*, 2003; *Montelli et al.*, 2004].

[6] The MER forms one arm of the complex Afar triple junction zone (Figure 2). Rifting initiated in the southern and central Main Ethiopian rift between 18 and 15 Ma but the northern Main Ethiopian rift only developed after ~11 Ma [*WoldeGabriel et al.*, 1990; *Wolfenden et al.*, 2004]. Between 12 and 10 Ma, the southern Red Sea margin propagated southward as the MER propagated NE, effectively linking the southern Red Sea and Ethiopian rifts, and

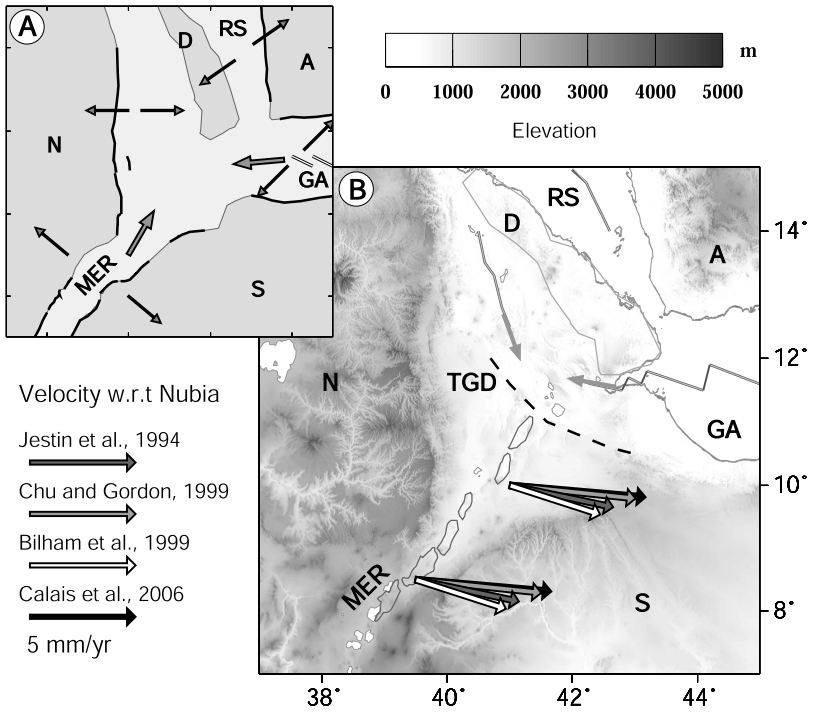

Figure 2. Past and present constraints on plate kinematics in the Afar triple junction zone. A, Arabia; D, Danakil; N, Nubian Plate; S, Somalian Plate; RS, Red Sea rift; GA, Gulf of Aden rift; MER, Main Ethiopian rift; TGD, Tendaho-Goba'ad Discontinuity. (a) Pre-3.2 Ma tectonics of the Afar triple junction. Relatively rigid blocks are shaded. Rift propagation directions are shown by light grey arrows. Thin dark grey arrows show pre-3.2 Ma extension directions. (b) The 3.2 Ma to present and current plate motions with respect to the Nubian plate; vector length scaled to extensional velocity. Along-axis propagation direction is shown by light grey arrows.

forming a triple junction for the first time [*Wolfenden et al.*, 2004].

[7] The northern Main Ethiopian rift is a series of linked half grabens bounded by steep NE striking Miocene border faults [*WoldeGabriel et al.*, 1990; *Wolfenden et al.*, 2004] (Figure 1). Structural patterns suggest a change from N130°E to N105°E directed extension sometime in the interval 6.6 to 3 Ma [*Boccaletti et al.*, 1998; *Wolfenden et al.*, 2004]. During this time period extensional strain migrated from border faults to smaller offset approximately N10°E striking faults and aligned eruptive centers in the central rift valley [*Wolfenden et al.*, 2004]. The <20 km wide, right-stepping, en echelon zones of magmatism and faulting are referred to as magmatic segments [*Ebinger and Casey*, 2001]. GPS measurements show that approximately 80% of present-day extension across the MER is localized within these magmatic segments [*Bilham et al.*, 1999]. The magmatic segments in the center of the rift are underlain by ~20-km-wide, high-velocity (V_p > 6.5 km/s) elongate bodies that are interpreted as cooled mafic intrusions [*Keranen et al.*, 2004; *Mackenzie et al.*, 2005]. These magmatic segments are characterized by relative positive Bouguer anomalies [*Mahatsente et al.*, 1999; *Tiberi et al.*, 2005]. Historic fissural basalt flows at Fentale and Kone volcanoes as recently as 1810 indicate ongoing volcanism in magmatic segments [*Harris*, 1844].

[8] The northern Main Ethiopian rift shows a northward increase in crustal extension and magmatic modification [*Tiberi et al.*, 2005; *Maguire et al.*, 2006; *Stuart et al.*, 2006]. Crustal thickness beneath the MER decreases from 38 km in the south beneath the caldera lakes to 24 km beneath Fentale volcano in the southern Afar depression [*Dugda et al.*, 2005; *Maguire et al.*, 2006] (Figure 1). The along-axis thinning is consistent with a northward along-axis decrease in effective elastic thickness and seismogenic layer thickness [*Ebinger and Hayward*, 1996]. Seismic refraction/wide-angle reflection data show ~40-km-thick crust beneath the southeastern plateau, whereas the western side of the rift is underlain by 45- to 50-km-thick crust with a ~10- to 15-km high-velocity lower crust believed to be underplate [*Mackenzie et al.*, 2005].

[9] Geochemical and seismic data provide constraints on melting and melt emplacement beneath the MER. The major element compositions of Quaternary mafic lavas from the MER show the onset of melting occurs in the lower crust and upper subcontinental lithospheric mantle [*Rooney et al.*, 2005]. This is consistent with *P* and *S* wave tomographic models that show anomalous low-velocity zones in the upper mantle beneath the rift, attributed to a combination of higher temperatures and the presence of partial melt [*Bastow et al.*, 2005]. Both the large amount of *SKS* splitting and the rift parallel orientation of the fast polarization direction led *Kendall et al.* [2005] to propose that partial melt beneath the MER rises through dikes that penetrate through the thinned lithosphere. Shear wave splitting in local earthquakes beneath the MER shows that anisotropy is highest in zones of diking, and it suggests that

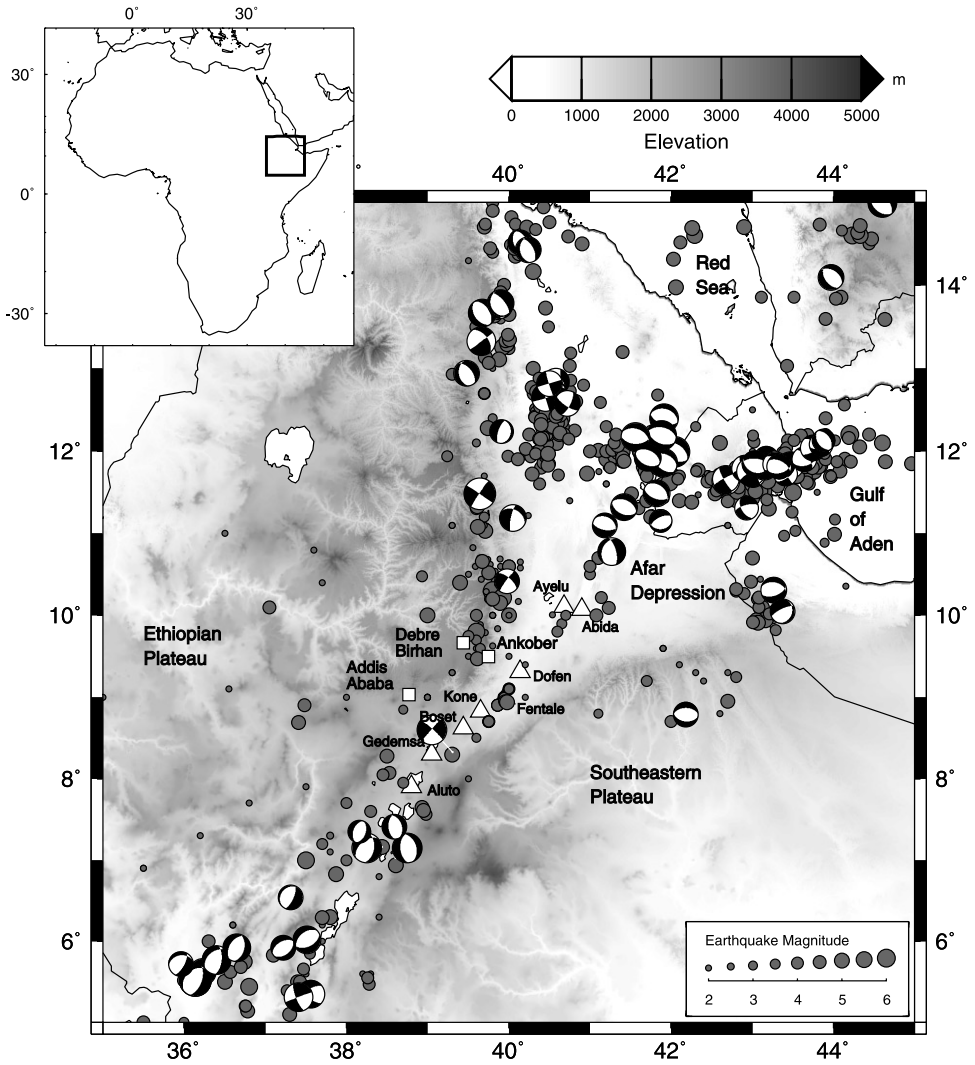

Figure 3. Seismic activity of the Horn of Africa since 1960. Earthquake locations and magnitudes are from *Ayele* [1995] for the time period 1960–1997 and the NEIC catalogue (1997–2005). Earthquake focal mechanisms are from Harvard CMT catalogue, *Foster and Jackson* [1998], *Ayele and Arvidsson* [1998], *Ayele* [2000], and *Hofstetter and Beyth* [2003]. Quaternary volcanoes in the MER are shown by triangles.

melt-induced anisotropy deeper in the lithosphere continues into the upper crust [*Keir et al.*, 2005].

[10] The orientation of present-day extension across the Ethiopian rift remains controversial. Laser ranging and GPS data show that the northern Ethiopian rift over the period 1969–1997 extended in a direction of N108°E ± 10° at 4.5 ± 0.1 mm/yr [*Bilham et al.*, 1999] (Figure 2). The velocity field calculated from permanent GPS stations on Africa since 1996 shows opening of ~6–7 mm/yr at an azimuth of approximately N95°E [*Fernandes et al.*, 2004; *Calais et al.*, 2006] (Figure 2). Global and regional plate tectonic models by *Jestin et al.* [1994] and *Chu and Gordon* [1999] average plate kinematic indicators from the past 3.2 Ma and find similar extension directions and extensional velocities of N102°E at 5 ± 1 mm/yr and N96°E ± 9° at 6.0 ± 1.5 mm/yr, respectively. Active Quaternary volcanoes in the MER have elliptical shapes with their long axes in the direction N105°E [*Casey et al.*, 2006]. Source parameters of teleseismically recorded earthquakes show normal, normal left-oblique and sinistral strike-slip motions with the horizontal component of *T* axes between N135°E and N90°E in orientation [e.g., *Ayele and Arvidsson*, 1998; *Foster and Jackson*, 1998; *Ayele*, 2000; *Hofstetter and Beyth*, 2003] (Figure 3). Kinematic indicators on Quaternary faults that dip 70–75° and strike N10–35°E indicate a principal dip-slip normal movement with a mean direction of approximately N95°E [*Pizzi et al.*, 2006]. However, *Acocella and Korme* [2002] matched pairs of asperities along the sides of Quaternary extension fractures to show a mean extension direction of N128°E ± 20°. *Korme et al.* [1997] used the orientation of extension fractures to determine an extension direction of NW-SE, similar to *Wolfenden et al.*'s [2004] N130°E estimate of Miocene-Pliocene extension direction.

3. Seismic Activity

[11] Seismicity data are lacking from the Ethiopian rift due to previous sparse station coverage [*Ayele and*

Kulhánek, 1997]. The earliest documented seismic event in the Ethiopian rift is a swarm of earthquakes in 1841–1842 near Debre Birhan which caused the destruction of the town of Ankober by landslides [*Gouin*, 1979] (Figure 3). Historical records spanning the past 150 years show that large magnitude earthquakes are rare in the MER [*Gouin*, 1979]. The record of seismicity from 1960 to 2000 compiled from teleseismic and regional catalogues complete down to $M_L \sim 4$ shows that the majority of earthquakes are located along the highly eroded southern Red Sea escarpment north of 9.5°N, 38.7°E [e.g., *Kebede et al.*, 1989; *Ayele*, 1995; *Ayele and Kulhánek*, 1997; *Hofstetter and Beyth*, 2003; *Ayele et al.*, 2006b] (Figure 3).

[12] An estimate of seismic moment release since 1960 shows that more than 50% of extension across the MER is accommodated aseismically [*Hofstetter and Beyth*, 2003]. During this period swarms of low-magnitude events have been located near Debre Birhan [*Gouin*, 1979], and near Fentale volcano in 1981 and 1989 where NNE striking surface fissures developed following earthquake swarms of $M_L < 4$ [*Asfaw*, 1982]. Similar fissures oriented N20°E and N45°E are observed elsewhere along the axis of the MER and attributed to tectonic processes [*Asfaw*, 1982, 1998]. Tension fractures cut welded tuffs at Fentale and Kone volcanoes and suggest a fissuring episode within the past 7000 years [*Williams et al.*, 2004]. In the year preceding this study, the seismicity was concentrated in the Fentale-Dofen and Angelele magmatic segments [*Ayele et al.*, 2006a]. From mid-October 2003, after removal of the EAGLE seismic network, a ~1 month long earthquake swarm with a main shock of $M_L \sim 5$ was recorded by the Geophysical Observatory and reported by local inhabitants near Dofen volcano (Geophysical Observatory, Addis Ababa University, personal communication). The epicenter of the main shock is estimated to be ~9.2°N 40.1°E from the locations of damaged buildings and trees, reported scree slides in the area, and personal accounts of ground shaking (Figure 3).

[13] Hypocenter depths of 5–10 km have been reported for seismic swarms in the MER and southern Afar [*Asfaw*, 1982; *Ayele et al.*, 2006a]. Teleseismically recorded earthquakes on the eastern side of the MER have been located between 8 and 12 km depth [*Ayele*, 2000].

4. EAGLE Seismic Data

4.1. Seismic Network

[14] Local earthquakes were recorded on 29 broadband seismic stations (EAGLE phase I) that were operational between late October 2001 and January 2003 (Figure 1). These three-component Güralp CMG-3T and CMG-40TD instruments recorded data at 50 Hz. Additional data over this time period was acquired from the permanent broadband stations AAE, FURI, and WNDE maintained by the Geophysical Observatory, Addis Ababa University. The number of seismic stations was increased during the final 4 months of the experiment with the deployment of an additional 50 CMG-6TD instruments recording at 100 Hz. These stations were deployed at ~15 km spacing in the rift valley and in the Ankober region, and were operational between October 2002 and February 2003 (EAGLE phase II). For security reasons the broadband stations were located in compounds attached to schools, clinics and plantation offices. A further 100 CMG-6TD instruments deployed at ~5 km spacing across the rift valley and adjacent plateaus were operational between November 2002 and January 2003 (EAGLE phase III). Three local earthquakes were recorded on up to ~600 single-component, short-period, Reftek "Texan" instruments deployed for 8 days at ~1 km spacing both along and across the rift valley. During the daytime, the level of high-frequency cultural noise (>1 Hz) could be high. At night, however, noise levels were significantly reduced.

4.2. Arrival Time Analysis

[15] Earthquakes were detected on the continuous seismic data of the phase I array with a short-term amplitude/long-term amplitude (STA/LTA) trigger algorithm with windows 1 s and 60 s in length respectively. The algorithm scanned the continuous data, filtered using a Butterworth filter with corner frequencies of 2–15 Hz, and flagged time windows when an STA/LTA ratio of 20 was exceeded within a 120 s time window on two or more stations. Arrival times of *P* and *S* phases were initially measured on phase I data filtered using the same Butterworth filter. Arrival times from phase II and phase III seismic stations were added to earthquakes that occurred during the respective operation periods of these arrays. Arrival times of *P* phases were assigned a quality factor of 0, 1, 2, or 3 according to estimated measurement errors of 0.05 s, 0.1 s, 0.15 s, and 0.2 s, respectively, and *S* wave quality factors of 0, 1, 2, and 3 were assigned to arrivals with estimated measurement errors of 0.1 s, 0.175 s, 0.25 s, and 0.3 s, respectively. A total of 13,388 *P* wave and 12,725 *S* wave arrivals were picked from 2139 local earthquakes.

5. Methodology

5.1. Earthquake Location and Magnitude

[16] In total, 2139 local earthquakes recorded at four or more stations were located with the Hypo2000 algorithm [*Klein*, 2002]. A one-dimensional (1-D) *P* wave velocity model and V_p/V_s ratio of 1.75, calculated from *P* and *S* wave traveltimes, were used for the initial earthquake locations. The weighting of arrival times was dependent on the quality factor assigned to the phase, with *P* wave quality factors of 0, 1, 2, and 3 given full (1), 0.75, 0.5, and 0.25 weights respectively. *S* waves were given half weighting relative to *P* waves of the same quality factor.

[17] The 1-D *P* wave velocity model and station corrections were determined by simultaneously relocating earthquakes and inverting for velocity structure with VELEST [*Kissling et al.*, 1995]. Only earthquakes with eight or more *P* arrivals, an azimuthal gap of less than 180°, and an epicentral distance to the nearest station of less than twice the focal depth were used to invert for the 1-D *P* wave velocity model. 280 earthquakes satisfied the selection criteria and can be considered as "well-located" earthquakes. Additional constraints on the 1-D *P* wave model were provided by the controlled source experiment [*Mackenzie et al.*, 2005].

[18] The 280 well-located earthquakes were subsequently relocated using a 3-D *P* wave velocity model determined with SIMULP [e.g., *Eberhart-Philips and Michael*, 1998; *Haslinger et al.*, 1999]. Hypocenter accuracy of the earthquakes was tested by relocating shots and randomly adjusting horizontal and vertical positions of hypocenters. From

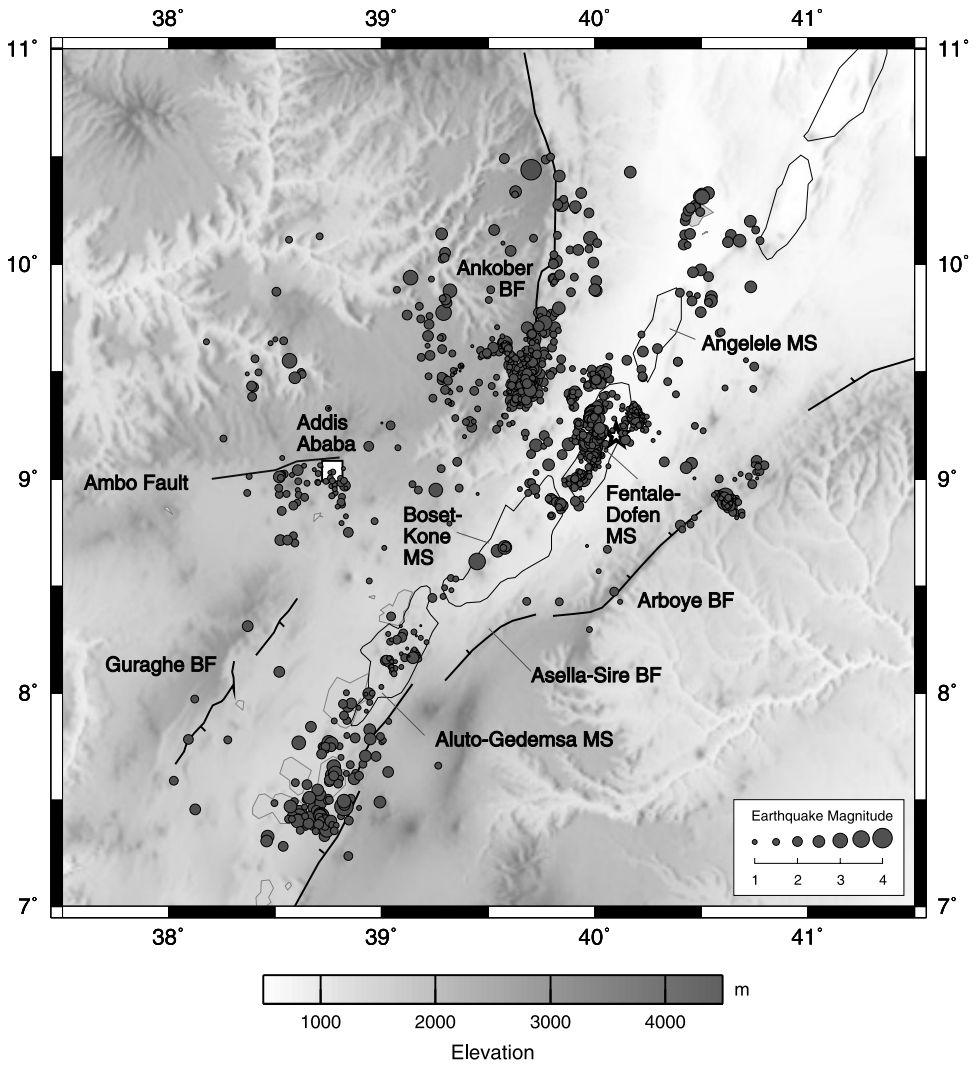

Figure 4. Seismicity of the MER from October 2001 to January 2003. Earthquakes were located with the minimum 1-D *P* wave velocity model determined from local earthquake tomography. Only events recorded by at least four stations and located within the array of seismic stations are displayed. Heavy black lines show major border faults; ellipses mark Quaternary magmatic segments. The star shows the location of the October 2003 earthquake swarm near Dofen volcano.

these tests we estimate hypocenter accuracy for earthquakes of about ±600 m in horizontal directions and ±2000 m in depth.

[19] Local magnitude was estimated using the maximum body wave displacement amplitudes (zero to peak) measured on a simulated Wood-Anderson seismograph and distance correction terms of *Hutton and Boore* [1987]. The power law cumulative frequency-magnitude distribution [*Gutenberg and Richter*, 1956] is used to describe the size distribution of earthquakes recorded within the EAGLE network in the MER. The *b* value is calculated using the maximum likelihood method [*Aki*, 1965]. The standard deviation of the *b* value is used as an error estimate [*Shi and Bolt*, 1982].

5.2. Focal Mechanisms and Stress Inversion

[20] Focal mechanisms were computed from *P* and *SH* wave polarities using the grid search algorithm FOCMEC [*Snoke et al.*, 1984]. A double-couple source type is assumed as all the events selected are characterized by high-frequency content, sharp first arrivals and clear *S* phases at the nearest stations. Hypocenter coordinates were determined by locating the event with the 3-D velocity model. A fault plane solution was only attempted if an earthquake was located within the network, the nearest station was within an epicentral distance of twice the focal depth, and the solution had a minimum of 10 *P* wave polarities located in at least three quadrants of the focal sphere. Polarity errors of neither *P* nor *SH* waves were tolerated in the grid search algorithm. In total, 33 well-constrained and unambiguous fault plane solutions that have a maximum 20° uncertainty in either strike or dip of both nodal planes were determined. This new data set is supplemented by the three well-constrained focal mechanisms determined from data at regional and teleseismic distances [*Ayele*, 2000; *Hofstetter and Beyth*, 2003] (CMT, Harvard).

[21] The focal mechanisms were used to invert for the regional stress tensor with the linear, least squares stress inversion method of *Michael* [1984] that minimizes the angle

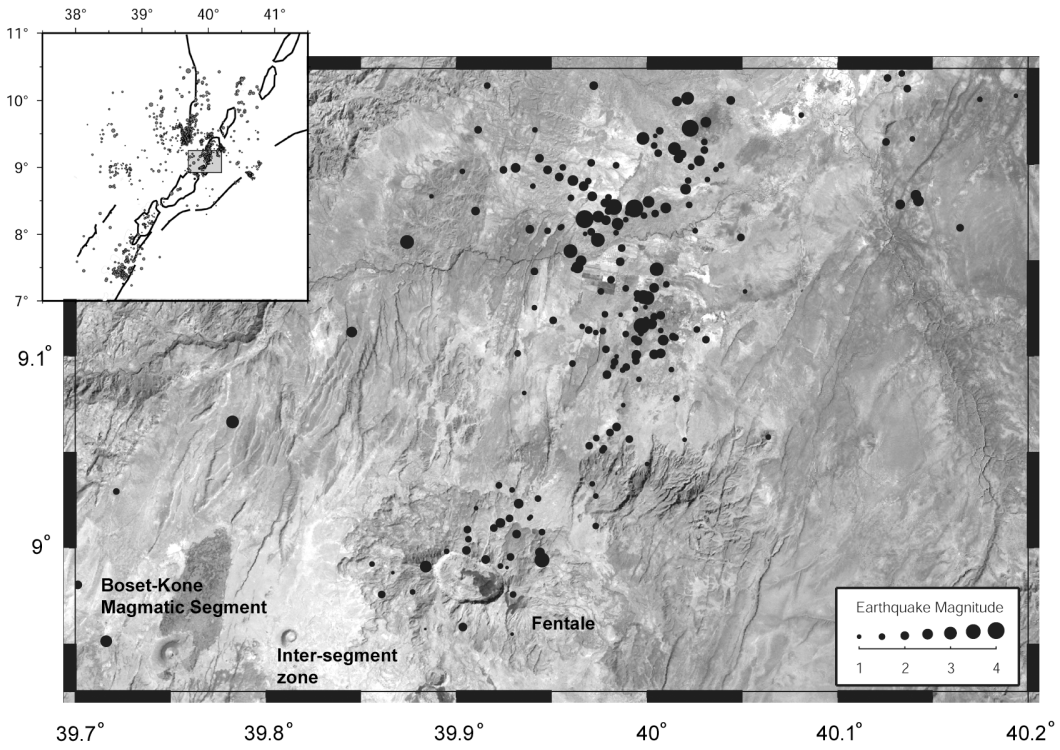

Figure 5. Example of seismicity located near Quaternary eruptive volcanic centers and faults of the Fentale-Dofen magmatic segment plotted on a gray scale Landsat 741 image. The inset shows the position of the image with respect to border faults and magmatic segments in the MER.

between the predicted tangential traction on the fault plane and the observed slip direction. The 95% confidence regions were determined with the bootstrap resampling method [*Michael*, 1987a, 1987b] and used as an error estimate. The relatively small data set and estimated focal mechanism errors of this study make this method most appropriate to both accurately determine the stress orientation and adequately estimate the confidence limits [*Hardebeck and Hauksson*, 2001].

[22] The inversion procedure assumes that the four stress parameters are constant over the spatial and temporal extent of the data set and that earthquakes slip in the direction of the resolved shear stress on the fault plane [*Michael*, 1984]. The uniform stress tensor that best explains the mechanisms is expressed by the three principal stress axes (where σ_1, σ_2 and σ_3 are the maximum, intermediate, and minimum principal stresses, respectively) and the stress ratio. An average misfit angle $\overline{\beta}$, which measures the difference between the observed slip direction and the predicted direction of maximum tangential traction, is computed and used as a measure of the success of the inversion. The steepest nodal plane of the normal fault focal mechanisms and approximately NE striking nodal planes of the strike-slip mechanisms were chosen as fault planes for the inversion in accord with geological observations [e.g., *Abebe et al.*, 1998a; *Wolfenden et al.*, 2004; *Casey et al.*, 2006; *Pizzi et al.*, 2006].

6. Results

6.1. Hypocenter Distribution

[23] From October 2001 to January 2003, 2139 local earthquakes were recorded by the EAGLE network. Of these, 1957 earthquakes were located within the network of seismic stations (Figure 4). Concentrated seismic activity occurs in the Fentale-Dofen magmatic segment, which is a 20-km-wide, 70-km-long zone that extends from Fentale caldera to Dofen volcano (Figure 4). Earthquakes are located in a 10-km-wide, NNE trending zone that extends 40 km north of Fentale volcano where the pattern of seismicity is mirrored by the surface expression of the closely spaced, small offset Quaternary faults and fractures (Figure 5). Three distinct earthquake clusters are located near the Pliocene–Recent Dofen volcano (Figures 4 and 6). The distribution of earthquakes located with the 3-D *P* wave velocity model show that these clusters are elongate approximately north to approximately NNE, parallel to the surface expression of major Quaternary fault systems that cut lavas erupted from fissures (Figure 6).

[24] The frequency-depth distribution of earthquakes within the Fentale-Dofen magmatic segment located with the 3-D *P* wave velocity model shows most earthquakes are 8–14 km deep (Figure 6 and 7). Hypocenter depths are 8–10 km deep near Fentale and Dofen volcanoes but are up to 16 km deep in between these major eruptive centers (Figure 6). The temporal distribution of seismicity in the Fentale-Dofen magmatic segment is characterized by earthquake swarms that punctuate largely aseismic periods (Figure 8).

[25] Minor seismicity is located within the Boset and Aluto-Gedemsa magmatic segments (Figure 4). Regions between the right stepping en echelon magmatic segments are largely aseismic.

[26] Seismic activity south of the Aluto-Gedemsa magmatic segment is more diffuse than to the north (Figure 4).

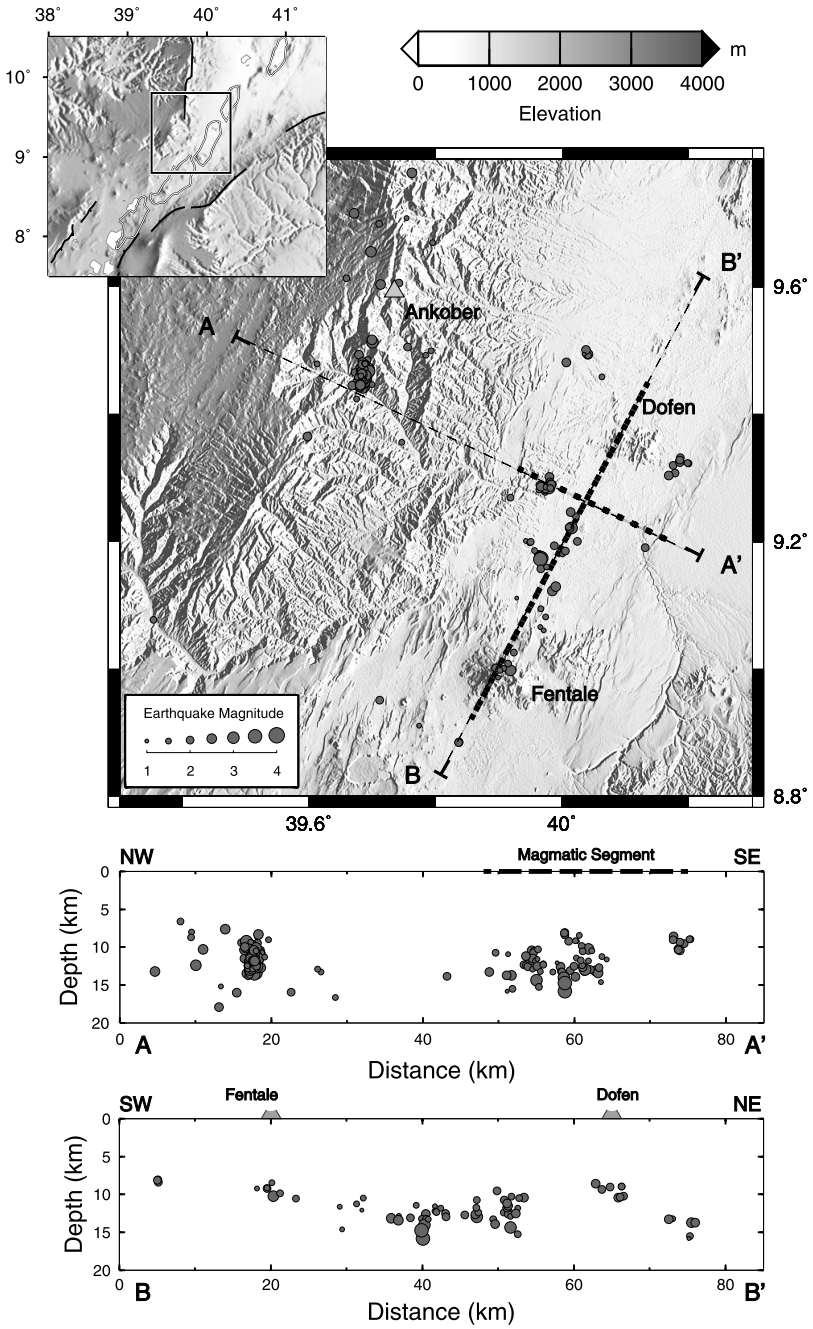

Figure 6. Earthquake locations determined using the 3-D *P* wave velocity model in the Ankober region and Fentale-Dofen magmatic segment, plotted on 90 m resolution SRTM topographic data. The earthquakes were recorded with eight or more *P* wave arrivals and have an azimuthal gap of less than 180° and an epicentral distance to the nearest station of less than twice the focal depth. From Ankober (grey triangle) south, the uplifted rift flank of the ~30 Ma southern Red Sea was warped southeastward into the northern MER after ~11 Ma. Profiles A-A′ and B-B′ project earthquakes within 30 km of the line of section onto the profile. The thickened portions of the profiles show where the profile crosses the Fentale-Dofen magmatic segment.

This rift sector lacks the narrow zone of localized faults and eruptive centers characterizing the magmatic segments (Figure 10). Epicenters are located within a 30- to 40-km-wide zone of Quaternary faults along the eastern side of the rift valley. The amount of seismicity in this rift sector is relatively low and lacks the periods of swarm activity observed further north in the Fentale-Dofen magmatic segment (Figure 8).

[27] The exception to the pattern of correlated seismicity and Quaternary eruptive centers is the long-lived seismicity at the intersection of the NE striking Miocene MER and north striking Oligocene Red Sea structures near Ankober

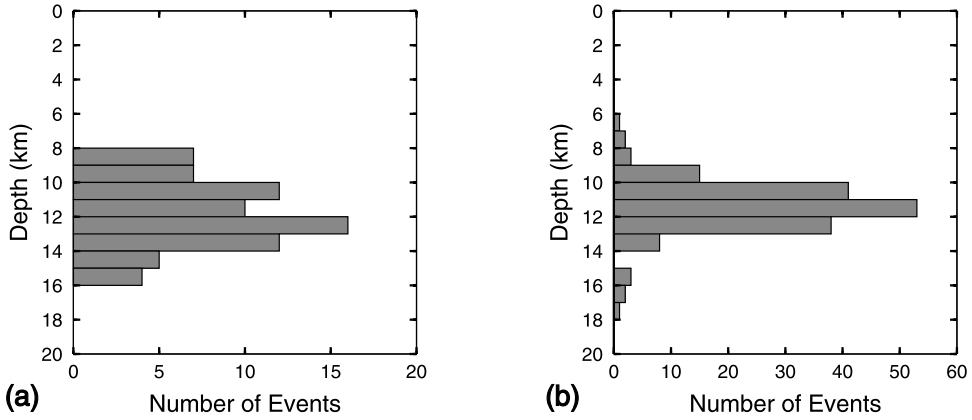

Figure 7. Histograms of number of earthquakes per 1 km depth bin interval for the (a) Fentale – Dofen magmatic segment and (b) Ankober region. The hypocenters were located with the 3-D *P* wave velocity model and are displayed on Figure 6.

(Figures 4 and 6). This intersection zone has the highest relief in the region, with deeply incised valleys. Earthquakes are localized in a N-S oriented cluster on the northwest margin of the rift valley at 9.5°N 39.75°E. The cluster lies at the southern end of the approximately north striking Ankober border fault system, which is a series of closely spaced high-angle normal faults and tight monoclinal folds [*Wolfenden et al.*, 2004]. The rate of seismicity in this area was high for the first 6 months of the experiment and characterized by frequent swarm activity (Figure 8). Focal depths are concentrated between 10 and 13 km with activity observed down to 18 km (Figures 6 and 7).

[28] A minor, roughly E-W elongate cluster of earthquakes is located near Addis Ababa (Figure 4). The structure of this area is dominated by the east striking Ambo lineament, a fault zone active since the late Miocene [*Abebe et al.*, 1998b]. Isolated but relatively deep earthquakes (15–21 km) characterize the remaining earthquake activity of the Ethiopian plateau. The southeastern plateau shows a lack of activity except for a small cluster on the southern margin of the Gulf of Aden rift at 9°N 40.5°E (Figure 4).

6.2. Seismicity Rate

[29] The annual cumulative frequency-magnitude distribution of the 1957 earthquakes recorded within the EAGLE network shows that the seismicity catalogue is complete above M_L 2.1 (Figure 9). The largest magnitude earthquake is only M_L 3.9. The estimated *b* value using the maximum likelihood method of *Aki* [1965] is 1.13 ± 0.05, and this slope intercepts the *y axis* at 4.5. This is the first reliable *b* value estimate for the MER as the historic record is too sparse for a reliable estimate [*Ayele and Kulhánek*, 1997]. *Hofstetter and Beyth* [2003] obtained a *b* value of 0.83 ± 0.08 for a larger area that encompasses both the MER and southern Ethiopian Rift to 5°N.

[30] The estimated *b* value of 1.13 ± 0.05 for the MER is similar to *b* values of between 1.05 and 1.3 calculated for the oceanic southern Red Sea and Gulf of Aden rift systems [*Ayele and Kulhánek*, 1997; *Hofstetter and Beyth*, 2003]. Lower *b* values of between 0.7 and 0.9 are observed in the less evolved continental rifts in Kenya and Tanzania [e.g., *Tongue et al.*, 1992; *Langston et al.*, 1998; *Ibs-von Seht et al.*, 2001].

6.3. Focal Mechanisms and Stress Inversion

[31] In total, 33 well-constrained and unambiguous fault plane solutions that have a maximum 20° uncertainty in either strike or dip of both nodal planes were determined (Table 1 and Figures 10 and 11). This new data set is supplemented by the three well-constrained focal mechanisms determined from data at regional and teleseismic distances [*Ayele*, 2000; *Hofstetter and Beyth*, 2003] (CMT, Harvard) (Table 2 and Figure 10).

[32] Focal mechanisms of earthquakes located along the axis of the MER and in the Ankober fault system show predominantly normal dip slip on steep faults that strike approximately north to approximately NNE (Figures 10 and 12). Focal mechanisms are subparallel to the dominant N10°E orientation of Quaternary faults in the Ethiopian rift [*Boccaletti et al.*, 1998; *Wolfenden et al.*, 2004; *Casey et al.*, 2006] (Figure 10). A few of the normal dip-slip focal mechanisms have slip planes that strike approximately NE, parallel to the pre-3.5 Ma, N40°E striking faults (Figure 12). The exceptions to these normal dip-slip focal mechanisms are the strike-slip earthquakes below Fentale and Boset volcanoes, interpreted as left-lateral motion on approximately NE to approximately ENE striking faults (Figure 12). However, both normal and strike-slip focal mechanisms show near horizontal *T* axes striking N80°E–N130°E (Figures 11 and 12).

[33] The results of the stress inversion using the 36 focal mechanisms in the MER show that the trend/plunge of the minimum principal stress is 283°/6° with a mean misfit angle ($\overline{\beta}$) ± standard deviation of 10.9° ± 7.0° (Figure 12). This mean misfit angle is comparable to results of stress tensor inversions from focal mechanisms within uniform stress fields in other studies: 10–17° along fault segments of the San Andreas fault zone [*Jones*, 1988]; and 6–24° for data sets in the Swiss Alps and northern Alpine foreland [*Kastrup et al.*, 2004]. However, a well-resolved stress tensor requires that the data set contains a diverse range of focal mechanisms. In our data set, only four strike-slip focal mechanisms differ from the predominant dip slip on approximately north to approximately NE striking faults.

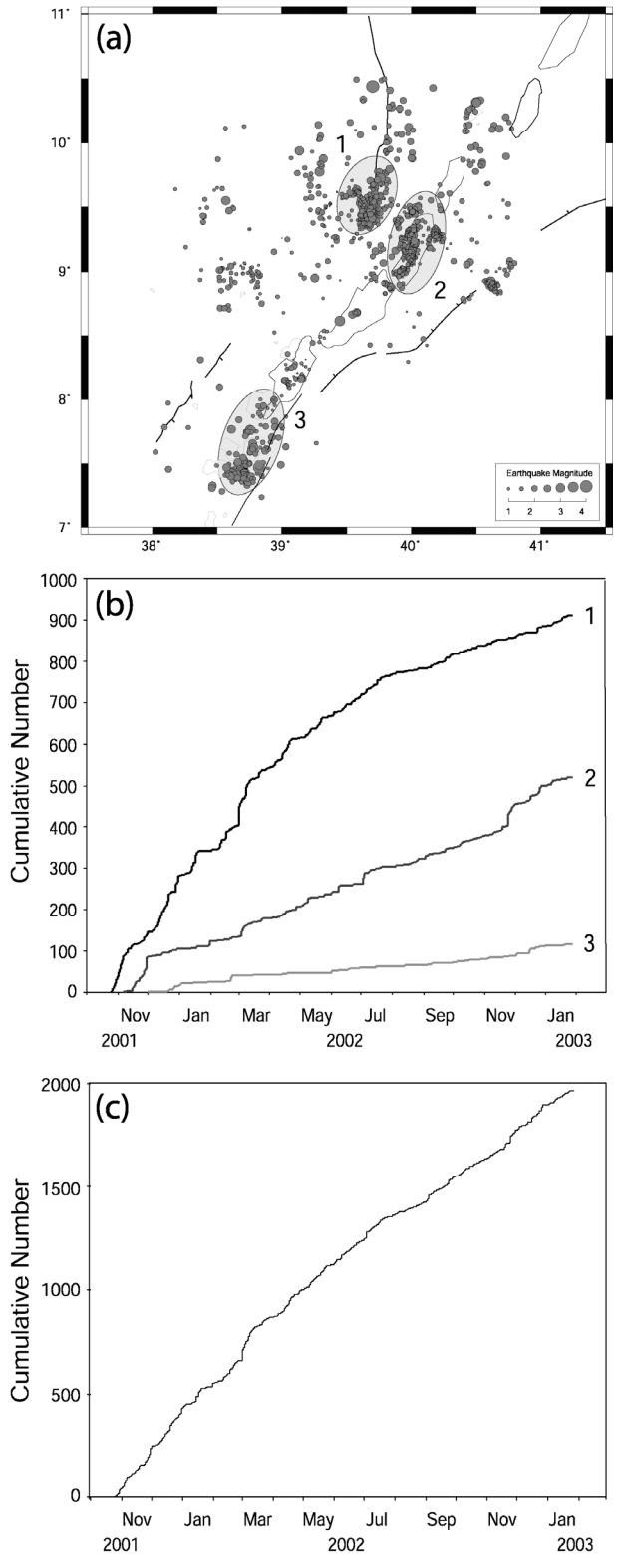

Figure 8. (a) Seismicity of the MER recorded by the EAGLE network with the three regions that experienced the most activity highlighted: 1, Ankober area; 2, Fentale-Dofen magmatic segment; and 3, south of Aluto-Gedemsa magmatic segment. (b) Cumulative number of earthquakes versus recording time of the regions 1, 2, and 3. (c) Cumulative number of earthquakes versus recording time of all the earthquakes recorded within the EAGLE network.

This unavoidable lack of diversity in type of focal mechanism reduces the resolution of the stress tensor.

7. Discussion

7.1. Distribution of Seismicity

[34] This study recorded seismicity for 15 months and thus provides a snapshot of active deformation in the MER. However, the pattern of Quaternary faults and fissures that cut recent lavas and historic seismicity data show that our results are representative of the longer-term brittle strain patterns in the rift [e.g., *Asfaw*, 1982, 1998; *Williams et al.*, 2004; *Wolfenden et al.*, 2004; *Ayele et al.*, 2006a; *Casey et al.*, 2006].

[35] The most striking feature of the recorded seismicity in the MER is the coincidence of earthquake swarms and the magmatic segments, which are the locus of Quaternary volcanism. The inactivity of mid-Miocene border faults that define the overall approximately NE trend of the rift is reflected in the minor geodetic strain on the rift flanks [*Bilham et al.*, 1999] and lack of large magnitude earthquakes on border faults over the last ~50 years [*Ayele and Kulhánek*, 1997]. This inactivity is inferred from historical records spanning the past 150 years [*Gouin*, 1979], and morphology of the border faults [*Boccaletti et al.*, 1998; *Wolfenden et al.*, 2004].

[36] The exception is the seismicity observed at the intersection between the north striking Red Sea rift and the NE striking MER. The cluster of earthquakes is located on the north striking Ankober fault system that formed at ~11 Ma to link the two oblique rift systems. Although fault and seismicity patterns show that the locus of strain has shifted to the Quaternary magmatic segments in the central rift, this high point along the rift flank still experiences strain [*Wolfenden et al.*, 2004]. The strike of the Ankober fault system is oblique to the NE trending MER, and

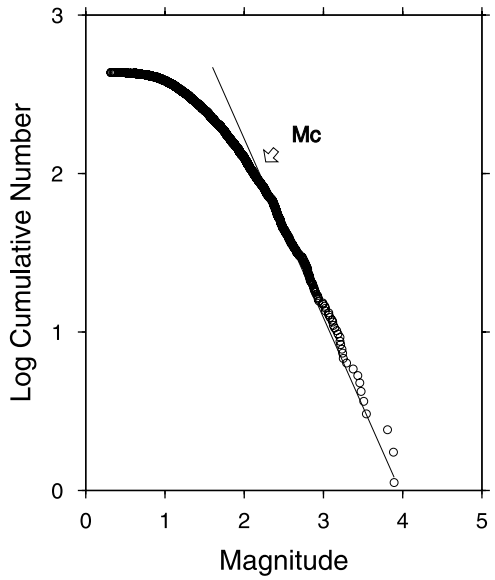

Figure 9. Log annual cumulative number of earthquakes against magnitude plot of earthquakes recorded within the EAGLE network. Mc marks M_L 2.1, above which the catalogue is complete. The slope of the straight line (b value) is 1.13 ± 0.05.

Table 1. Earthquake Source Parameters Determined From EAGLE Data

Event	Date, year/month/day	Time, UT	Latitude, °N	Longitude, °E	Depth, km	Strike	Dip	Rake	M_L
1	2002/01/16	2122:39.44	9.239	40.021	13.25	180.00	50.00	−90.00	1.7
2	2002/01/17	0138:03.91	8.154	39.002	20.29	2.27	60.05	−93.46	2.01
3	2002/01/18	0142:40.83	8.998	39.918	10.23	359.67	54.23	−97.40	2.82
4	2002/02/17	0238:15.44	9.470	39.692	11.86	171.52	66.00	−90.00	3.21
5	2002/05/02	2143:23.17	9.122	39.984	13.16	211.58	56.38	−80.38	2.64
6	2002/07/04	0259:42.35	9.173	39.966	15.84	214.40	60.08	−85.38	3.54
7	2002/07/31	0154:38.27	9.444	39.677	11.25	172.76	66.06	−85.62	2.34
8	2002/08/21	0127:23.93	8.951	39.711	13.85	192.88	60.13	−84.23	2.14
9	2002/10/08	1937:43.42	9.199	39.949	12.65	225.74	68.06	−85.69	2.03
10	2002/10/09	1819:37.91	9.193	39.987	12.52	223.13	68.19	−64.02	2.14
11	2002/10/10	1915:51.93	9.066	39.965	14.59	201.49	58.30	−66.30	1.17
12	2002/10/19	2125:25.96	10.130	39.957	15.47	198.07	59.38	−71.32	2.83
13	2002/11/04	0017:42.49	8.432	39.673	12.91	2.54	51.18	−83.58	1.17
14	2002/11/04	0024:55.49	7.812	38.976	6.88	183.82	63.32	−109.10	1.71
15	2002/11/05	2242:14.69	9.728	39.370	14.65	29.29	66.39	−79.08	1.92
16	2002/11/07	0124:31.21	9.492	40.040	15.48	216.30	46.04	−74.63	1.89
17	2002/12/03	1602:52.26	7.481	38.553	13.63	183.71	68.01	−92.16	2.55
18	2002/12/03	2010:01.33	7.700	38.911	12.43	190.00	45.00	−90.00	2.34
19	2002/12/04	1341:09.57	8.873	39.836	9.57	209.92	60.00	−90.00	1.97
20	2002/12/13	1736:21.66	9.494	40.034	15.79	183.69	64.27	−98.89	2.2
21	2002/12/15	0837:35.26	7.428	38.648	8.61	197.95	50.00	−90.00	3.06
22	2002/12/15	1915:38.82	7.430	38.657	6.42	210.49	70.38	−78.31	2.89
23	2002/12/15	2035:05.22	9.548	40.144	19.01	190.55	66.56	−103.10	1.93
24	2002/12/17	2212:36.10	9.001	39.907	8.44	64.49	88.17	−0.81	1.4
25	2002/12/17	2315:10.76	8.998	39.901	9.17	71.95	80.73	−3.78	1.55
26	2002/12/23	0627:49.95	9.446	39.680	10.43	181.99	60.00	−90.00	2.45
27	2002/12/26	1947:51.98	9.221	40.014	12.96	213.15	62.02	−87.74	3.17
28	2002/12/26	1955:17.90	9.221	40.011	12.65	219.89	60.00	−90.00	2.41
29	2003/01/02	0852:45.37	9.246	40.013	13.91	195.00	65.00	−90.00	2.37
30	2003/01/10	1213:56.08	8.611	39.447	7.00	42.64	85.25	13.19	3.44
31	2003/01/13	2106:00.76	9.491	39.681	11.17	168.45	56.21	−97.23	1.97
32	2003/01/20	2116:22.90	7.475	38.823	11.74	206.12	42.96	−104.76	2.52
33	2003/01/21	0808:18.85	7.495	38.822	11.41	197.78	37.16	−117.15	2.9

focused deformation in this complex zone of rift intersection may be caused by flexure accommodating differential subsidence in the Red Sea rift relative to the younger MER. Further north of Ankober, the Red Sea rift margin is seismically active as shown in historical records, regional catalogues and recent seismicity [*Ayele et al.*, 2006b]. Stress is concentrated in this area by the large lateral density contrast and difference in lithospheric thickness between the uplifted western Ethiopian plateau and Afar depression [e.g., *Dugda et al.*, 2005; *Tiberi et al.*, 2005].

[37] A number of lines of evidence indicate that extensional strain is accommodated by a combination of dike injection and faulting within magmatic segments, as outlined below. For the period 1960–2000, a comparison of the expected released seismic moment and observed seismic moment shows that less than 50% of extension across the MER is accommodated by rapid slip on faults [*Hofstetter and Beyth*, 2003]. At the surface, GPS measurements show that approximately 80% of present-day extension across the MER is localized in a ~20-km-wide zone of Quaternary faulting and magmatism [*Bilham et al.*, 1999]. This narrow zone of localized deformation is also observed in the brittle upper crust from patterns of seismicity. Elongate clusters of earthquakes are associated with observed faults, fissures and active eruptive centers in the Fentale-Dofen magmatic segment. The swarms of low-magnitude earthquakes are concentrated at 8–14 km depth which coincides with the top of the ~20- to 30-km-wide zone of extensive mafic intrusions at 8–10 km depth [*Keranen et al.*, 2004]. Seismic anisotropy of the upper crust is highest in the magmatic segments and attributed to melt-filled cracks and dikes aligned perpendicular to the minimum stress [*Keir et al.*, 2005]. Crustal strain across the MER is accommodated within the magmatic segments by magma intrusion below ~10 km, and by both faulting and dike intrusion in the brittle seismogenic zone.

[38] The Debre Zeit and Butajira chains of Quaternary eruptive centers located west of the magmatic segments are largely aseismic, and they show little structural or morphological evidence of active strain. Xenolith data and tomographic models show these chains are underlain by hot asthenosphere [*Bastow et al.*, 2005; *Rooney et al.*, 2005], but they lack the large relative positive Bouguer anomaly and high-velocity crust of the magmatic segments [e.g., *Tiberi et al.*, 2005]. These chains may be either unfavorably oriented "failed" magmatic segments, or incipient zones of strain.

[39] In the magmatic segments of the MER, seismicity, geodetic and structural data all show a localization of strain in zones of Quaternary magmatism. The earthquakes in the magmatic segments are concentrated above axial mafic intrusions and may be induced by dike injection. Models of the elastic stress field surrounding propagating fluid-filled cracks show that earthquakes of magnitude >1 can be induced ahead of a propagating dike if the ambient stress field is near to failure, and slip is likely to occur along preexisting fractures [*Rubin and Gillard*, 1998]. Earthquake swarms are assumed to occur near the crack tips due to the increasing stress caused by concentrated internal fluids. Spatially, swarms reflect areas of magma intrusion. The correlation we observe in the MER between seismic swarms and magma injection has been documented near active volcanoes in other settings, suggesting the swarms are causally linked to magma intrusion. For example, seismicity

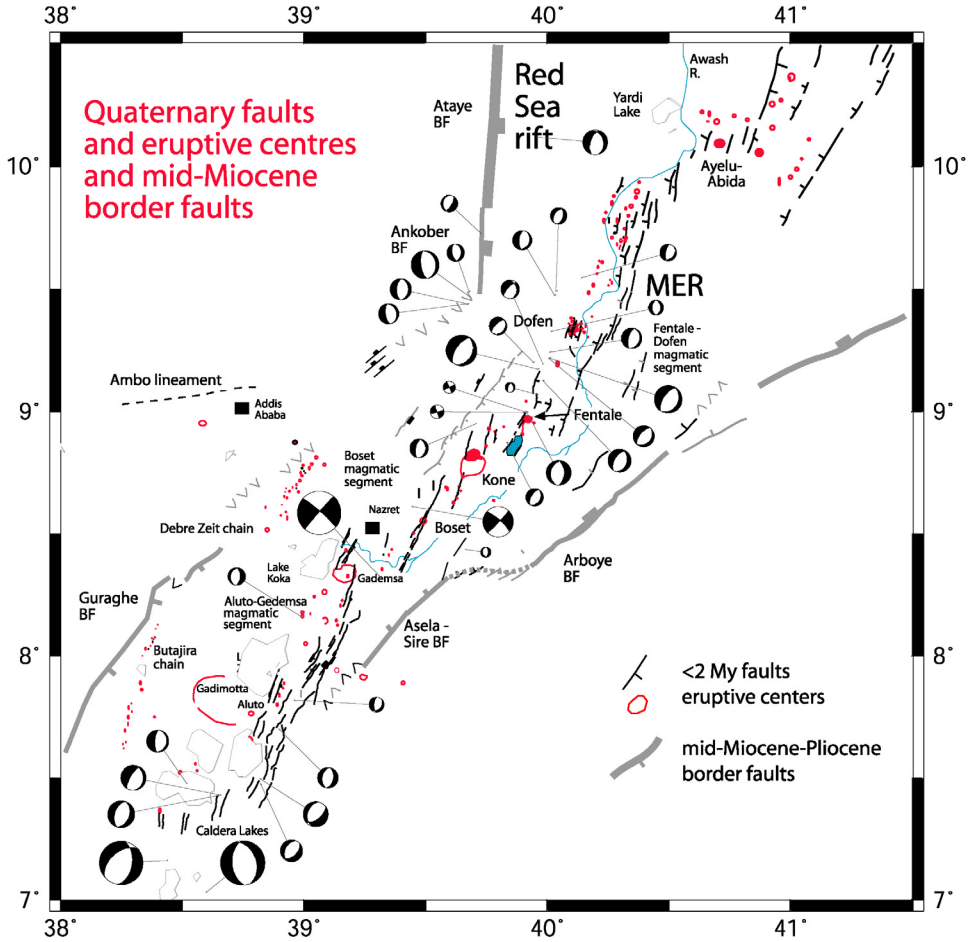

Figure 10. Faults that cut <1.9 Ma lavas, and Quaternary eruptive centers comprising magmatic segments, relative to the Miocene border faults bounding Main Ethiopian rift basins [after *Casey et al.*, 2006]. Fault plane solutions are lower hemisphere projections. The size of the solution is scaled to magnitude between M_L 1.17 and 5.3.

leading to the Mount Etna eruption of 2001 was characterized by swarms elongate parallel to surface fractures and parallel to the maximum compressive stress determined from focal mechanisms [*Musumeci et al.*, 2004]. This seismic activity was interpreted as being caused by dike emplacement prior to the eruption. By analogy to these other locales and independent data from the MER, we propose that the observed seismicity in magmatic segments above axial mafic intrusions is induced by magma injection into the midcrust to upper crust (Figure 13).

[40] The along-axis segmentation of the MER is reflected at the surface by the right-stepping en echelon patterns of Quaternary faults and aligned cones within discrete 20-km-wide, 60-km-long magmatic segments. The pattern of seismicity interpreted in light of other data provides clues as to the origin of this along-axis segmentation. At 8–10 km depth subsurface, the segmentation is evident as discrete axial mafic intrusions imaged by crustal tomography [*Keranen et al.*, 2004]. These mafic bodies correlate with along-axis velocity variations in the midcrust and lower crust, implying that mafic intrusions extend to the base of the crust [*Maguire et al.*, 2006]. Extension in the midcrust to lower crust is thus likely accommodated within a narrow zone of magma injection. The onset of melting likely occurs in the lower crust and subcontinental lithosphere [*Rooney et al.*, 2005]. The correlation between the orientation of lithospheric anisotropy and the distribution of Quaternary strain and magmatism shows that vertically oriented dikes with partial melt crosscut the lithosphere [*Kendall et al.*, 2005]. The concentrated seismicity in the Fentale-Dofen magmatic segment and largely aseismic Boset-Kone and Aluto-Gedemsa magmatic segments is indirect evidence that episodic rifting events within one magmatic segment are independent of other magmatic segments. This suggests magma source regions are spatially and temporally discrete.

[41] The pattern of seismicity observed in the MER is strikingly similar to patterns in oceanic rift zones where seismic swarms are induced in already stressed lithosphere by injection of magma. For example, seismic swarms in the Hengill volcanic area in southwestern Iceland are concentrated at the base of the seismogenic layer and have predominantly double-couple mechanisms [*Feigl et al.*, 2000]. Calculations of Coulomb failure stress suggest that magma injection to ~7 km subsurface is sufficient to trigger earthquakes in the overlying crust. Clusters of seismicity marked a narrow zone parallel to fissure swarms in the Krafla spreading segment of northern Iceland 5–8 years after a dike injection episode [*Arnott and Foulger*, 1994].

This pattern was attributed to the release of stress as the crust returns to equilibrium in the neighborhood of the new dikes [*Arnott and Foulger*, 1994]. Alternatively, *Cattin et al.* [2005] reproduce geodetic observations constrained by heat flow and seismicity in the Asal-Ghoubbet rift using a viscoelastic model of semicontinuous dike intrusion in a narrow zone at depth. Episodes of magma injection explain the localized seismicity patterns and high slip rates on faults close to the rift axis, as well as geodetically measured ground deformation.

7.2. Style of Faulting and Extension Direction

[42] The focal mechanisms provide a uniform picture for the pattern of faulting and stress field orientation of the Ethiopian rift. Focal mechanisms indicate predominantly normal dip slip on faults that strike approximately north to approximately NNE, parallel to the dominant N10°E strike of faults that cut Quaternary lavas [e.g., *Casey et al.*, 2006]. Field observations and geodetic data of volcanic rift zones in Iceland and Hawaii indicate that dike intrusions are most often associated with normal faulting and fracturing at the surface [*Rubin*, 1992]. The predominance of normal dip slip, and resulting lack of diversity in our focal mechanism data set, is thus consistent with dike-induced seismicity in the MER.

[43] The normal, oblique, and left-lateral strike-slip displacement on NE striking fault planes most likely occurs on pre-3.5 Ma, N40°E striking faults that probably formed under a NW-SE extension direction. These have most likely been reactivated as N40°E striking ramps and transfer faults to link N10°E striking fault segments formed under the approximately N105°E extension direction during the Quaternary [*Wolfenden et al.*, 2004; *Casey et al.*, 2006]. The negligible block rotations about vertical axes in zones in between magmatic segments suggests no throughgoing transform faults have developed, thus supporting our interpretation of the strike-slip focal mechanisms as left-lateral approximately NE striking faults [*Kidane et al.*, 2006].

[44] The N103°E orientation of the minimum compressive stress from focal mechanisms parallels, within errors, the geodetically determined extension direction averaged over the past 3.2 Myr [*Jestin et al.*, 1994; *Chu and Gordon*, 1999] and current extension direction determined from campaign and permanent GPS data [*Bilham et al.*, 1999; *Fernandes et al.*, 2004; *Calais et al.*, 2006]. Extension is perpendicular to the strike of Quaternary faults, fissures and aligned cones and is in agreement with structural studies that show a WNW-ESE direction of extension during Quaternary times [*Boccaletti et al.*, 1998; *Wolfenden et al.*, 2004; *Casey et al.*, 2006]. The current direction of extension is thus perpendicular to the strike of Quaternary volcanic chains and faults in the magmatic segments. The right-stepping en echelon pattern at the surface may be induced by approximately N105°E directed extension above an approximately NE striking low-velocity zone in the upper mantle connecting the MER to the triple junction in Afar [*Benoit et al.*, 2003; *Bastow et al.*, 2005].

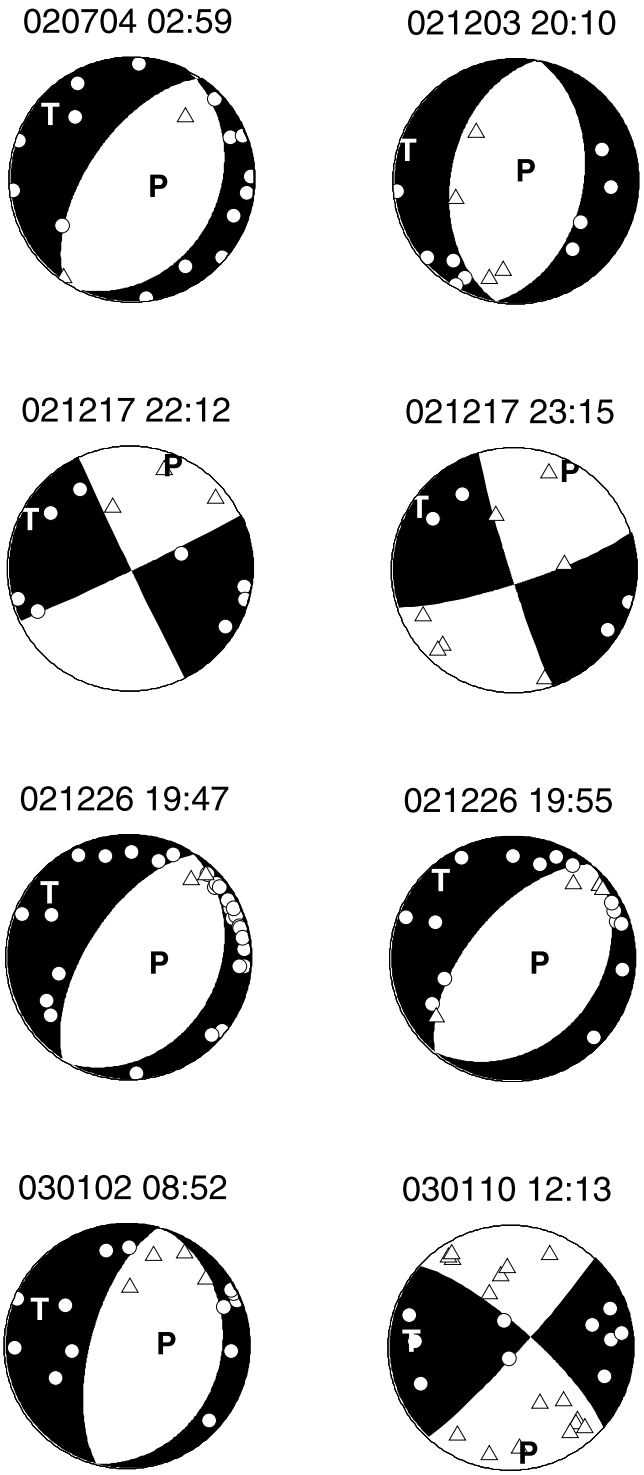

Figure 11. A selection of focal mechanisms from this study. Compressional *P* wave first motions are plotted as circles and dilational first motions are plotted as triangles. The compressional quadrants of the focal sphere are shaded black. Each solution is labeled by earthquake origin time GMT (year, month, day, hour, minute).

8. Conclusions

[45] 1. From October 2001 to January 2003, 1957 earthquakes were located within the EAGLE network of broad-

Table 2. Earthquake Source Parameters Determined in Other Studies

Event	Date, year/month/day	Time, UT	Latitude, °N	Longitude, °E	Strike	Dip	Rake	M_w	Data Source
34	1983/12/28	2308	7.03	38.60	176	51	−81	5.3	Harvard CMT
35	1993/02/13	0225	8.33	39.91	221	87	−7	4.9	*Ayele* [2000]
36	1995/01/20	0714	7.16	38.44	9	49	−119	5.0	*Hofstetter and Beyth* [2003]

band seismic stations in the northern Main Ethiopian rift and on its uplifted rift flanks. The earthquake catalogue is complete above M_L 2.1 and the b value is 1.13 ± 0.05.

[46] 2. Excluding the MER-Red Sea rift intersection zone at Ankober, seismicity within the rift is localized to <20-km-wide, right-stepping, en echelon zones of Quaternary magmatism. Seismicity in these magmatic segments is characterized by swarms of low-magnitude earthquakes located in clusters that parallel Quaternary faults, fissures and chains of eruptive centers. The earthquakes in the magmatic segments are predominantly <14 km deep and may be triggered by dike injection.

[47] 3. Seismic activity at Ankober may be caused by flexure accommodating differential subsidence at the oblique intersection of the <11 Ma MER and the older Red Sea rift.

[48] 4. Earthquake focal mechanisms show predominantly normal dip slip on faults striking approximately north to approximately NNE. The orientation of the minimum compressive stress determined from focal mechanisms is N103°E, consistent with geodetic data and global plate kinematic constraints.

[49] 5. From integration of these results with other geophysical and structural observations we propose that present-day extension in the MER is localized to discrete <20-km-wide en echelon magmatic segments, where extensional strain in the upper crust is accommodated by both dike intrusion and dike induced faulting. The individual

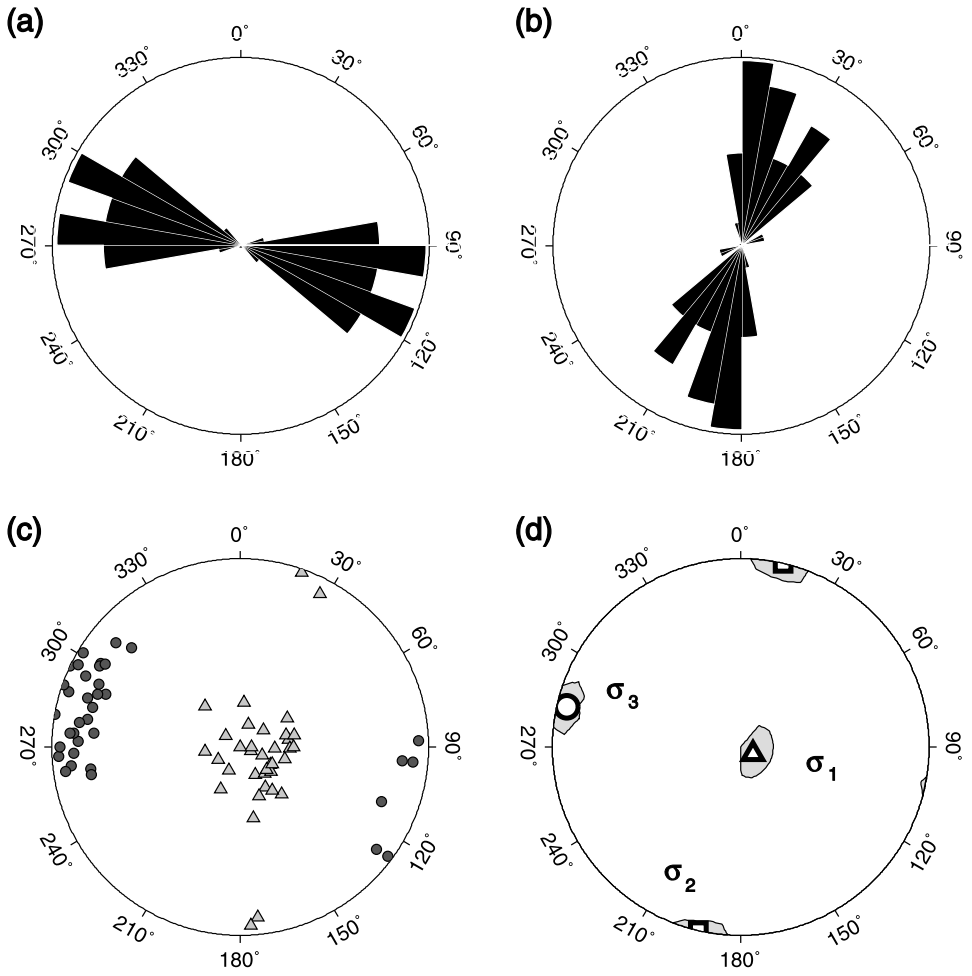

Figure 12. (a) Rose diagram of the orientation of the T axes of earthquake focal mechanisms. (b) Rose diagram showing the strike of earthquake slip planes. (c) Lower hemisphere plot of the trend and plunge of fault plane solution T axes (dark circles) and P axes (light triangles). (d) Results of the stress tensor inversion. Circle shows σ_3, the minimum compressive stress. Square shows σ_2, the intermediate compressive stress. Triangle shows σ_3, the maximum compressive stress. The 95% confidence limits are shown by regions of grey shading.

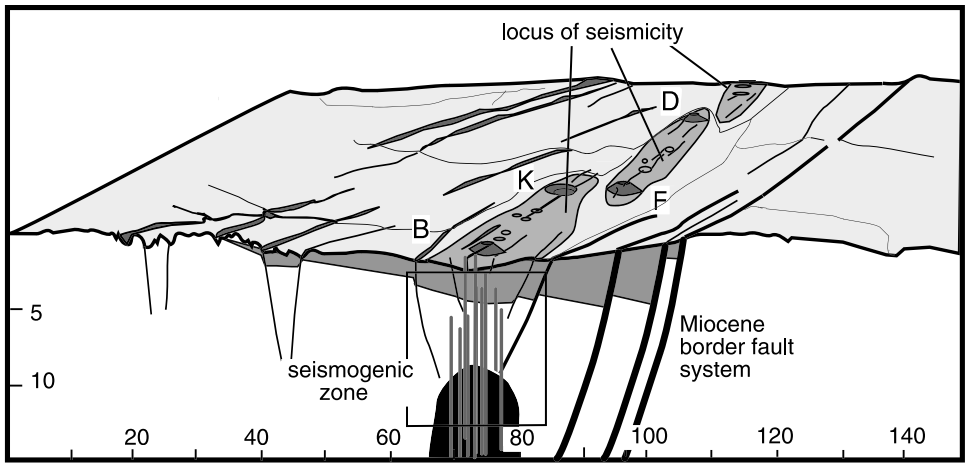

Figure 13. Cartoon sketch of the MER that shows abandoned Miocene border faults and localization of strain in <20-km-wide right-stepping en echelon magmatic segments that are zones of Quaternary magma intrusion and faulting. Front face is constrained by topographic relief along the line of EAGLE controlled source seismic profiles. Letters mark volcanoes: B, Boset; K, Kone; F, Fentale; D, Dofen.

magmatic segments show large spatial and temporal variations in level of seismicity over the time period of the study, suggesting magma source regions for separate magmatic segments are spatially and temporally discrete.

[50] **Acknowledgments.** We thank SEIS-UK for the use of instruments and A. Brisbourne for assistance in the field, with data management and analysis. We thank A. Page, C. Tiberi, and A. Intawong for help with data acquisition and processing. D. Cornwell, I. Bastow, and M. Casey are thanked for their significant contributions to this study. Laike Asfaw, Bekele Abebe, Dereje Ayalew, Gezahegn Yirgu, and Tesfaye Kidane of Addis Ababa University are thanked for support throughout the project. We thank Stephanie Prejean, Kevin Furlong, and an anonymous reviewer who helped improve this manuscript. Our research was supported by NERC grant NER/A/S/2000/01004 and NERC studentship NER/S/A/2002/10547.

References

Abebe, B., M. Boccaletti, R. Mazzuoli, M. Bonini, L. Tortorici, and T. Trua (1998a), Geological map of the Lake Ziway-Asela region (Main Ethiopian Rift), scale 1:50,000, Cons. Naz. delle Ric., A. R. C. A. Florence, Italy.

Abebe, T., F. Mazzarini, F. Innocenti, and P. Manetti (1998b), The Yerer-Tullu Wellel volcanotectonic lineament: A transtensional structure in central Ethiopia and the associated magmatic activity, *J. Afr. Earth Sci.*, *26*(1), 135–150.

Acocella, V., and T. Korme (2002), Holocene extension direction along the Main Ethiopian Rift, East Africa, *Terra Nova*, *14*, 191–197.

Acocella, V., T. Korme, and F. Salvini (2003), Formation of normal faults along the axial zone of the Ethiopian Rift, *J. Struct. Geol.*, *25*, 503–513.

Aki, K. (1965), Maximum likelihood estimate of *b* in the formula log N = a − *b*M and its confidence limits, *Bull. Earthquake Res. Inst. Univ. Tokyo*, *43*, 237–239.

Arnott, S. K., and G. R. Foulger (1994), The Krafla spreading segment, Iceland: 1. Three-dimensional crustal structure and the spatial and temporal distribution of local earthquakes, *J. Geophys. Res.*, *99*(B12), 23,801–23,825.

Asfaw, L. M. (1982), Development of earthquake induced fissures, *Nature*, *286*, 551–553.

Asfaw, L. M. (1998), Environmental hazard from fissures in the Main Ethiopian Rift, *J. Afr. Earth Sci.*, *27*(3/4), 481–490.

Ayele, A. (1995), Earthquake catalogue of the Horn of Africa for the period 1960–1993, *Rep. 3-95*, pp. 1–9, Seismol. Dep., Uppsala Univ., Uppsala.

Ayele, A. (2000), Normal left-oblique fault mechanisms as an indication of sinistral deformation between the Nubia and Somalia plates in the Main Ethiopian Rift, *J. Afr. Earth Sci.*, *31*(2), 359–368.

Ayele, A., and R. Arvidsson (1998), Fault mechanisms and tectonic implication of the 1985–1987 earthquake sequence in south western Ethiopia, *J. Seismol.*, *1*, 383–394.

Ayele, A., and O. Kulhánek (1997), Spatial and temporal variation of the seismicity in the Horn of Africa from 1960–1993, *Geophys. J. Int.*, *130*, 805–810.

Ayele, A., G. W. Stuart, I. D. Bastow, and D. Keir (2006a), The August 2002 earthquake sequence in north Afar: Insights into the neotectonics of the Danakil microplate, *J. Afr. Earth Sci.*, in press.

Ayele, A., A. A. Nyblade, C. A. Langston, M. Cara, and J.-J. Leveque (2006b), New evidence for Afro-Arabian plate separation in southern Afar, in *The Structure and Evolution of the East African Rift System in the Afar Volcanic Province*, edited by G. Yirgu, C. J. Ebinger, and P. K. H. Maguire, *Geol. Soc. Spec. Publ.*, *259*, in press.

Bastow, I. D., G. W. Stuart, J.-M. Kendall, and C. J. Ebinger (2005), Upper mantle seismic structure in a region of incipient continental breakup: Northern Ethiopian rift, *Geophys. J. Int.*, *162*, 479–493.

Benoit, M. H., A. A. Nyblade, J. C. VanDecar, and H. Gurrola (2003), Upper mantle *P* wave velocity structure and transition zone thickness beneath the Arabian Shield, *Geophys. Res. Lett.*, *30*(10), 1531, doi:10.1029/2002GL016436.

Bilham, R., R. Bendick, K. Larson, P. Mohr, J. Braun, S. Tesfaye, and L. Asfaw (1999), Secular and tidal strain across the Main Ethiopian Rift, *Geophys. Res. Lett.*, *26*, 2789–2792.

Boccaletti, M., M. Bonini, R. Mazzuoli, B. Abebe, L. Piccardi, and L. Tortorici (1998), Quaternary oblique extensional tectonics in the Ethiopian Rift (Horn of Africa), *Tectonophysics*, *287*, 97–116.

Buck, W. R. (2004), Consequences of asthenospheric variability on continental rifting, in *Rheology and Deformation of the Lithosphere at Continental Margins*, edited by G. D. Karner et al., pp. 1–30, Columbia Univ. Press, New York.

Calais, E., C. DeMets, and J.-M. Nocquet (2003), Evidence for a post-3.16–Ma change in Nubia-Eurasia-North America plate motions, *Earth Planet. Sci. Lett.*, *216*, 81–92.

Calais, E., C. Ebinger, C. Hartnady, and J. M. Nocquet (2006), Kinematics of the East African rift from GPS and earthquake slip vector data, in *The Structure and Evolution of the East African Rift System in the Afar Volcanic Province*, edited by G. Yirgu, C. J. Ebinger, and P. K. H. Maguire, *Geol. Soc. Spec. Publ.*, *259*, in press.

Casey, M., C. Ebinger, D. Keir, R. Gloaguen, and F. Mohamed (2006), Strain accommodation in transitional rifts: Extension by magma intrusion and faulting in Ethiopian rift magmatic segments, in *The Structure and Evolution of the East African Rift System in the Afar Volcanic Province*, edited by G. Yirgu, C. J. Ebinger, and P. K. H. Maguire, *Geol. Soc. Spec. Publ.*, *259*, in press.

Cattin, R., C. Doubre, J.-B. de Chabalier, G. King, C. Vigny, J.-P. Avouac, and J.-C. Ruegg (2005), Numerical modelling of Quaternary deformation and post-rifting displacement in the Asal-Ghoubbet rift (Djibouti, Africa), *Earth Planet. Sci. Lett.*, *239*, 352–367.

Chu, D., and R. G. Gordon (1999), Evidence for motion between Nubia and Somalia along the Southwest Indian Ridge, *Nature*, *398*, 64–67.

Debayle, E., J.-J. Lévêque, and M. Cara (2001), Seismic evidence for a deeply rooted low velocity anomaly in the upper mantle beneath the northeastern Afro/Arabian continent, *Earth Planet. Sci. Lett.*, *193*, 423–436.

Dugda, M., A. Nyblade, J. Julia, C. Langston, C. A. Ammon, and S. Simiyu (2005), Crustal structure in Ethiopia and Kenya from receiver function analysis: Implication for rift development in eastern Africa, *J. Geophys. Res.*, *110*, B01303, doi:10.1029/2004JB003065.

Dunbar, J., and D. Sawyer (1989), How pre-existing weaknesses control the style of continental breakup, *J. Geophys. Res.*, *94*, 7278–7292.

Eberhart-Philips, D., and A. J. Michael (1998), Seismotectonics of the Loma Prieta, California, region determined from three-dimensional V_p, V_p/V_s, and seismicity, *J. Geophys. Res.*, *103*, 21,099–21,120.

Ebinger, C., and M. Casey (2001), Continental breakup in magmatic provinces: An Ethiopian example, *Geology*, *29*, 527–530.

Ebinger, C. J., and N. Hayward (1996), Soft plates and hot spots: Views from Afar, *J. Geophys. Res.*, *101*, 21,859–21,876.

Ebinger, C., and N. Sleep (1998), Cenozoic magmatism throughout East Africa resulting from impact of a single plume, *Nature*, *395*, 788–791.

Feigl, K. L., J. Gasperi, F. Sigmundsson, and A. Rigo (2000), Crustal deformation near Hengill volcano, Iceland 1993–1998: Coupling between magmatic activity and faulting inferred from elastic modeling of satellite radar interferograms, *J. Geophys. Res.*, *105*, 25,655–25,670.

Fernandes, R., B. Ambrosius, R. Noomen, L. Bastos, L. Combrinck, J. Miranda, and W. Spakman (2004), Angular velocities of Nubia and Somalia from continuous GPS data: Implications on present-day relative kinematics, *Earth Planet. Sci. Lett.*, *222*, 197–208.

Foster, A. N., and J. A. Jackson (1998), Source parameters of large African earthquakes: Implications for crustal rheology and regional kinematics, *Geophys. J. Int.*, *134*, 422–448.

George, R., N. Roger, and S. Kelley (1998), Earliest magmatism in Ethiopia: Evidence for two mantle plumes in one flood basalt province, *Geology*, *26*, 923–926.

Gouin, P. (1979), *Earthquake History of Ethiopia and the Horn of Africa*, 258 pp., Int. Dev. Res. Centre, Ottawa, Ont.

Gutenberg, B., and C. F. Richter (1956), Earthquake magnitude, intensity, energy, and acceleration, *Bull. Seismol. Soc. Am.*, *46*, 105–145.

Hardebeck, J. L., and E. Hauksson (2001), Stress orientations obtained from earthquake focal mechanisms: What are appropriate uncertainty estimates, *Bull. Seismol. Soc. Am.*, *91*, 250–262.

Harris, W. C. (1844), *The Highlands of Ethiopia*, vol. 3, Longman, New York.

Haslinger, F., E. Kissling, J. Ansorge, D. Hatzfeld, E. Papadimitriou, V. Karakostas, K. Makropoulos, H.-G. Kahle, and Y. Peter (1999), 3D crustal structure from local earthquake tomography around the Gulf of Arta (Ionian region, NW Greece), *Tectonophysics*, *304*, 201–218.

Hayward, N., and C. Ebinger (1996), Variations in along-axis segmentation of the Afar rift system, *Tectonics*, *15*, 244–257.

Hofmann, C., V. Courtillot, F. Feraud, and P. Rochette (1997), Timing of the Ethiopian flood event: Implications for plume birth and global change, *Nature*, *389*, 838–841.

Hofstetter, R., and M. Beyth (2003), The Afar Depression: Interpretation of the 1960–2000 earthquakes, *Geophys. J. Int.*, *155*, 715–732.

Hutton, L. K., and D. M. Boore (1987), The M_L scale in southern California, *Bull. Seismol. Soc. Am.*, *77*, 2074–2094.

Ibs-von Seht, M., S. Blumenstein, R. Wagner, D. Hollnack, and J. Wohlenberg (2001), Seismicity, seismotectonics and crustal structure of the southern Kenya Rift: New data from the Lake Magadi area, *Geophys. J. Int.*, *146*, 439–453.

Jestin, F., P. Huchon, and J. M. Gaulier (1994), The Somalia plate and the East African Rift System: Present-day kinematics, *Geophys. J. Int.*, *116*, 637–654.

Jones, L. M. (1988), Focal mechanisms and the state of stress on the San Andreas fault in southern California, *J. Geophys. Res.*, *93*, 8869–8891.

Kastrup, U., M. L. Zoback, N. Deichmann, K. F. Evans, D. Giardini, and A. J. Michael (2004), Stress field variation in the Swiss Alps and the northern Alpine foreland derived from inversion of fault plane solutions, *J. Geophys. Res.*, *109*, B01402, doi:10.1029/2003JB002550.

Kebede, F., W.-Y. Kim, and O. Kulhánek (1989), Dynamic source parameters of the March–May 1969 Serdo earthquakes in central Afar, Ethiopia, deduced from teleseismic body waves, *J. Geophys. Res.*, *94*, 5603–5614.

Keir, D., J.-M. Kendall, C. J. Ebinger, and G. W. Stuart (2005), Variations in late syn-rift melt alignment inferred from shear-wave splitting in crustal earthquakes beneath the Ethiopian rift, *Geophys. Res. Lett.*, *32*, L23308, doi:10.1029/2005GL024150.

Kendall, J.-M., G. W. Stuart, C. J. Ebinger, I. D. Bastow, and D. Keir (2005), Magma assisted rifting in Ethiopia, *Nature*, *433*, 146–148.

Keranen, K., S. L. Klemperer, R. Gloaguen, and Eagle Working Group (2004), Three-dimensional seismic imaging of a protoridge axis in the Main Ethiopian rift, *Geology*, *32*, 949–952.

Kidane, T., E. Platzman, C. Ebinger, B. Abebe, and P. Rochette (2006), Paleomagnetic constraints on Continental Breakup: Observations from the Main Ethiopian rift, in *The Structure and Evolution of the East African Rift System in the Afar Volcanic Province*, edited by G. Yirgu, C. J. Ebinger, and P. K. H. Maguire, *Geol. Soc. Spec. Publ.*, *259*, in press.

Kieffer, B., et al. (2004), Flood and shield basalts from Ethiopia: Magmas from the African superswell, *J. Petrol.*, *45*(4), 793–834.

Kissling, E., U. Kradolfer, and H. Maurer (1995), VELEST user's guide: Short introduction, Inst. of Geophys. and Swiss Seismol. Serv., ETH, Zurich.

Klein, F. W. (2002), User's guide to Hypoinverse-2000, a FORTRAN program to solve for earthquake locations and magnitudes, *U.S. Geol. Surv. Open File Rep.*, *02-171*, 1–123.

Korme, T., J. Chorowicz, B. Collet, and F. F. Bonavia (1997), Volcanic vents rooted on extension fractures and their geodynamic implications in the Ethiopian Rift, *J. Volcanol. Geotherm. Res.*, *79*, 205–222.

Langston, C. A., R. Brazier, A. A. Nyblade, and T. J. Owens (1998), Local magnitude scale and seismicity rate for Tanzania, East Africa, *Bull. Seismol. Soc. Am.*, *88*, 712–721.

Lister, G., M. Etheridge, and P. Symonds (1986), Detachment faulting and the evolution of passive continental margins, *Geology*, *14*, 246–250.

Mackenzie, G. H., G. H. Thybo, and P. Maguire (2005), Crustal velocity structure across the Main Ethiopian Rift: Results from 2-dimenional wide-angle seismic modelling, *Geophys. J. Int.*, *162*, 996–1006.

Maguire, P. K. H., et al. (2003), Geophysical project in Ethiopia studies continental breakup, *Eos Trans. AGU*, *84*, 337, 342–343.

Maguire, P. K. H., et al. (2006), Crustal structure of the northern Main Ethiopian Rift from the EAGLE controlled source survey; a snapshot of incipient lithospheric break-up, in *The Structure and Evolution of the East African Rift System in the Afar Volcanic Province*, edited by G. Yirgu, C. J. Ebinger, and P. K. H. Maguire, *Geol. Soc. Spec. Publ.*, *259*, in press.

Mahatsente, R., G. Jenztsch, and T. Jahr (1999), Crustal structure of the Main Ethiopian Rift from gravity data: 3-dimensional modelling, *Tectonophysics*, *313*, 363–382.

Michael, A. J. (1984), Determination of stress from slip data: Faults and folds, *J. Geophys. Res.*, *89*, 11,517–11,526.

Michael, A. J. (1987a), The use of focal mechanisms to determine stress: A control study, *J. Geophys. Res.*, *92*, 357–368.

Michael, A. J. (1987b), Stress rotation during the Coalinga aftershock sequence, *J. Geophys. Res.*, *92*, 7963–7979.

Montelli, R., G. Nolet, F. A. Dahlen, G. Masters, E. R. Engdahl, and S.-H. Hung (2004), Finite-frequency tomography reveals a variety of plumes in the mantle, *Science*, *303*, 338–343.

Musumeci, C., O. Cocina, P. De Gori, and D. Patanè (2004), Seismological evidence of stress induced by dike injection during the 2001 Mt. Etna eruption, *Geophys. Res. Lett.*, *31*, L07617, doi:10.1029/2003GL019367.

Pizzi, A., M. Coltorti, B. Abebe, L. Disperati, G. Sacchi, and R. Salvini (2006), The Wonji Fault Belt (Main Ethiopian Rift, Ethiopia): Structural and geomorphological constraints and GPS monitoring, in *The Structure and Evolution of the East African Rift System in the Afar Volcanic Province*, edited by G. Yirgu, C. J. Ebinger, and P. K. H. Maguire, *Geol. Soc. Spec. Publ.*, *259*, in press.

Rooney, T. O., T. Furman, G. Yirgu, and D. Ayalew (2005), Structure of the Ethiopian lithosphere: Xenolith evidence in the Main Ethiopian Rift, *Geochem. Cosmochim. Acta*, *69*, 3889–3910.

Rubin, A. M. (1992), Dike-induced faulting and graben subsidence in volcanic rift zones, *J. Geophys. Res.*, *97*, 1839–1858.

Rubin, A. M., and D. Gillard (1998), Dike-induced earthquakes: Theoretical considerations, *J. Geophys. Res.*, *103*, 10,017–10,030.

Schilling, J.-G. (1973), Afar mantle plume: Rare earth evidence, *Nature*, *242*, 2–5.

Shi, Y., and B. A. Bolt (1982), The standard error of the magnitude-frequency *b*-value, *Bull. Seismol. Soc. Am.*, *72*, 1677–1687.

Snoke, J. A., A. C. Munsey, A. C. Teague, and G. A. Bollinger (1984), A program for focal mechanism determination by combined use of polarity and *SV-P* amplitude ratio data, *Earthquake Notes*, *55*(3), 15.

Stuart, G. W., I. D. Bastow, and C. J. Ebinger (2006), Crustal structure of the northern Main Ethiopian rift from receiver function studies, in *The Structure and Evolution of the East African Rift System in the Afar Volcanic Province*, edited by G. Yirgu, C. J. Ebinger, and P. K. H. Maguire, *Geol. Soc. Spec. Publ.*, *259*, in press.

Tiberi, C., C. Ebinger, V. Ballu, G. Stuart, and B. Oluma (2005), Inverse models of gravity data from the Red Sea - Aden - East African rifts triple junction zone, *Geophys. J. Int.*, *163*(2), 775–787, doi:10.1111/j.1365-246X.2005.02710.x.

Tongue, J. A., P. K. H. Maguire, and P. Burton (1992), Seismicity distribution from temporary earthquake recording networks in Kenya, *Tectonophysics*, *204*, 71–79.

Ukstins, I., P. Renne, E. Wolfenden, J. Baker, and M. Menzies (2002), Matching conjugate volcanic rifted margins: $^{40}Ar/^{39}Ar$ chrono-stratigraphy of pre- and syn-rift bimodal flood volcanism in Ethiopia and Yemen, *Earth Planet. Sci. Lett.*, *198*, 289–306.

Williams, F. M., M. A. J. Williams, and F. Aumento (2004), Tensional fissures and crustal extension rates in the northern part of the Main Ethiopian Rift, *J. Afr. Earth Sci.*, *38*, 183–197.

WoldeGabriel, G., J. Aronson, and R. Walter (1990), Geology, geochronology, and rift basin development in the central sector of the Main Ethiopian rift, *Geol. Soc. Am. Bull.*, *102*, 439–458.

Wolfenden, E., C. Ebinger, G. Yirgu, A. Deino, and D. Ayalew (2004), Evolution of the northern Main Ethiopian Rift: Birth of a triple junction, *Earth Planet. Sci. Lett.*, *224*, 213–228.

Wolfenden, E., C. Ebinger, G. Yirgu, P. Renne, and S. P. Kelley (2005), Evolution of the southern Red Sea rift: Birth of a magmatic margin, *Geol. Soc. Am. Bull.*, *117*, 846–864.

A. Ayele, Geophysical Observatory, Addis Ababa University, P.O. Box 1176, Addis Ababa, Ethiopia.

E. Daly, Department of Earth and Ocean Sciences, National University of Ireland, Galway, UK.

C. J. Ebinger and D. Keir, Department of Geology, Royal Holloway University of London, Egham TW20 0EX, UK. (d.keir@gl.rhul.ac.uk)

G. W. Stuart, School of Earth and Environment, University of Leeds, Leeds LS2 9JT, UK.